

Systematic of fusion incompleteness in reactions induced by α cluster projectiles

Sabir Ali,^{1,*} Kamal Kumar,² Muntazir Gull,^{2,†} Tauseef Ahmad,² I. A. Rizvi,² Avinash Agarwal,³
A. K. Chaubey,⁴ and S. S. Ghugre⁵

¹MANUU Polytechnic Darbhanga, Maulana Azad National Urdu University, Hyderabad 500 032, India

²Department of Physics, Aligarh Muslim University, Aligarh (U.P.) 202 002, India

³Department of Physics, Bareilly College, Bareilly (U.P.) 243 005, India

⁴Department of Physics, Addis Ababa University, P.O. Box 1176, Addis Ababa, Ethiopia

⁵UGC-DAE Consortium for Scientific Research, Kolkata 700 098, India



(Received 8 June 2019; revised manuscript received 28 October 2019; published 19 December 2019)

In order to investigate the systematic of fusion incompleteness in reactions induced by α cluster projectiles, a detailed study was carried out using the $^{20}\text{Ne} + ^{165}\text{Ho}$ system at energies above the barrier. Measurements of the excitation function (EF) of the observed evaporation residues (ERs) were carried out by employing the offline characteristic γ -ray detection method. The EFs of the ERs populated through xn/pxn channels were found to be in good agreement with the prediction of the statistical model code PACE4, whereas the EF of the ERs populated through the α emitting channels shows an enhancement over the PACE4 prediction. The degree of fusion incompleteness in the $^{20}\text{Ne} + ^{165}\text{Ho}$ reaction is estimated by comparing the fusion EF with coupled channels calculations and the extracted fusion function with the universal fusion function. The influence of input angular momentum on fusion reaction dynamics is explored in light of the sum-rule model. An attempt has also been made to examine the dependence of incomplete fusion probability on various entrance channel parameters.

DOI: [10.1103/PhysRevC.100.064607](https://doi.org/10.1103/PhysRevC.100.064607)

I. INTRODUCTION

During the last few decades, the study of fusion reactions using α cluster projectiles has caused resurgent interest in the study of heavy ion (HI) induced reactions [1–3]. Fusion reactions induced by medium and heavy mass α cluster projectiles result in bulk mass transfer from projectile to target through various fusion processes. When bombarded, the incident projectile may fuse with the target nucleus as a single entity, leading to complete mass and energy transfer through the direct complete fusion (DCF) process. However, it is also possible that the incident projectile may break up into fragments, due to excessive Coulomb repulsion, prior to fusion with the target nucleus. Sequential complete fusion (SCF) leads to fusion of all the breakup fragments of the incident projectile with the target nucleus, one after the other. On the other hand, the incomplete fusion (ICF) process involves the fusion of only a part of the incident projectile with the target nucleus. SCF and DCF are two aspects of the same reaction leading to the formation of a compound nucleus with the same degree of momentum and energy transferred and hence cannot be distinguished. Thus, the total complete fusion (CF) cross section is the algebraic sum of SCF and DCF i.e., $\sigma_{\text{CF}} = \sigma_{\text{SCF}} + \sigma_{\text{DCF}}$, while the total fusion (TF) cross section is the sum of CF and ICF cross sections, $\sigma_{\text{TF}} = \sigma_{\text{CF}} + \sigma_{\text{ICF}}$.

Among the various potential fusion processes in HI induced reactions, CF and ICF were found to be the most dominant at energies of 4–7 MeV/nucleon [4,5]. CF and ICF processes can be differentiated on account of the quantum of linear momentum being transferred from the incident projectile to the resulting compound system [6,7]. The CF process involves the total amalgamation of the incident projectile with the target nucleus, leading to complete transfer of incident momentum and energy to the intervening compound system. On the other hand, the ICF process leads to a fractional transfer of incident momentum and energy to the resulting compound system through the partial fusion of the incident projectile with the target nucleus. Since the inception of the ICF process, after the first observation of forward emitted fast light particle spectra by Britt and Quinton [8], numerous studies have been carried out involving a variety of projectile-target combination [9–12]. However, a consistent appreciation of the projectile breakup process only emerged with the work of Inamura *et al.* by performing the particle/ γ -ray coincidence measurement of the projectile-like fragments [13]. The breakup probability of the incident projectile, leading to the ICF reaction, was found to be governed by various entrance channel parameters, namely mass asymmetry of the projectile-target system, breakup threshold energy ($E_{\text{B.U.}}$) of the incident projectile, deformation parameter, and Coulomb repulsion between the incident projectile and the target nucleus [14–17].

Experimentally, it is difficult to measure the CF and ICF cross sections separately as various evaporation residues (ERs) populated in the course of irradiation are likely to have

*Corresponding author: sabir@manuu.ac.in

†muntazirgull1@gmail.com

contributions arising from the CF as well as ICF processes. However, ERs populated through different fusion processes can be identified directly by performing the particle/ γ -ray coincidence measurement [18]. The extent of contribution arising from CF and/or ICF processes in the population of a given ER can also be approximated directly by measuring the forward recoil range distribution (FRRD) of the populated residues [19]. Another method, which is utilized in the present work, for estimating the degree of fusion incompleteness involves comparison of the experimentally measured fusion excitation function (EF) and the extracted CF function with the predictions of coupled channels (CC) calculations and the universal fusion function (UFF) [20], respectively. In our previous work [2] we have measured the FRRDs of ERs populated in the $^{20}\text{Ne} + ^{51}\text{V}$ reaction and noted a suppression of $\approx 22\%$ in the CF function with respect to UFF. It will be interesting to study the role of various entrance channel parameters—namely mass asymmetry, Coulomb repulsion, and $E_{B,U}$ value of the incident projectile—on fusion suppression, by using the heavier mass target (^{165}Ho) with the same incident projectile (^{20}Ne). As the measurement of fusion cross sections for ^{20}Ne induced reactions with targets from different mass regions have already been carried out [16,21,22], a comparative study of the present and previously published data is likely to shed some light on the systematic of fusion suppression.

It is worthwhile to mention here that previously Singh *et al.* [23] also studied the $^{20}\text{Ne} + ^{165}\text{Ho}$ system at $E_{\text{lab}} \approx 88\text{--}164$ MeV and utilized the statistical model code PACE2 [24] to deduce the ICF fraction. The reported values of ICF fraction ($\approx 50\%$) in Ref. [23] were exceptionally high as far as the $E_{B,U}$ value of the incident projectile ^{20}Ne ($E_{B,U} = 4.73$ MeV) is concerned. In the present work coupled channels calculations were performed using the code CCFULL [25], which were proved to be a benchmark for estimating the ICF fraction. Observed ICF fractions were further cross verified by extracting the CF function from the experimentally measured CF cross sections and comparing with the UFF. Furthermore, values of critical angular momentum were extracted from the measured CF cross sections and compared with the theoretical values calculated using the code CCFULL. The main objective of the present work is to explore the various aspects of the ICF reaction dynamics and their dependence on entrance channel parameters: mass asymmetry, $E_{B,U}$ value of the incident projectile, and Coulomb repulsion between the projectile and target. The present work is organized as follows: Experimental details related to the present work are given in Sec. II. Analysis and interpretation of the results are discussed in Sec. III. Finally, the conclusion drawn from the present work is given in Sec. IV.

II. EXPERIMENTAL DETAILS

A. Target preparation and irradiation

The experiment was performed using the $^{20}\text{Ne}^{6+}$ ion beam at $E_{\text{lab}} \approx 145$ MeV from the K130 cyclotron at the Variable Energy Cyclotron Centre (VECC), Kolkata, India. Target foils interspersed with Al-degrader foils were placed in the form of a stack. Combinations of ^{165}Ho target and Al-degrader

foils were placed normal to the beam axis so that the ^{165}Ho target foil faces the incident beam followed by a stack of Al-degrader and target foils. Irradiation of the stack comprising target and the degrader foils was carried out in a specially designed vacuum chamber. The thickness of each Al-degrader and target foil was determined prior to use by weighing as well as by α transmission method. The thickness of Al-degrader foils was found to vary from 2.06 to 3.78 mg/cm² whereas the thickness of the ^{165}Ho target foils ranged from 1.30 to 1.56 mg/cm². The incident energy of the $^{20}\text{Ne}^{6+}$ ion beam on different target foils was calculated from the energy degradation of the initial beam energy using the code Stopping and Range of Ions in Matter (SRIM) [26]. Thicknesses of the Al-degrader and the target foils were taken in such a manner that the excitation function of the $^{20}\text{Ne} + ^{165}\text{Ho}$ system spanned an energy range of $E_{\text{lab}} \approx 90\text{--}145$ MeV. The $^{20}\text{Ne}^{6+}$ ion beam was collimated to a spot of diameter 8 mm. Keeping in mind the half-lives of interest, target foils were irradiated with an average beam current of ≈ 30 nA for ≈ 11 h. The weighted average beam current behind the target-degrader assembly was calculated by noting the total charge collected in the electron suppressed Faraday cup.

B. Post irradiation analysis and identification of the residues

Following the irradiation of the target foils, γ -ray activity induced in each of the target foils was recorded using a high purity germanium (HPGe) detector (having an active volume of 60 cc) coupled to a PC based data acquisition system developed by the VECC. Prior to recording the induced activity, the HPGe detector was calibrated using a standard γ -ray source, ^{152}Eu . The induced γ -ray activity in each of the target foils was recorded several times starting immediately after the stopping of beam current and continuing for a few days, at an interval ranging from 5 minutes to several hours. The resolution of the HPGe detector was found to be 2.5 keV for a 1408 keV γ -ray from the ^{152}Eu source. The activity of the observed ERs populated in the $^{20}\text{Ne} + ^{165}\text{Ho}$ reaction at $E_{\text{lab}} \approx 90\text{--}145$ MeV, listed in Table I, was extracted from the recorded γ -ray spectra. A typical recorded γ -ray energy spectrum of the ERs populated in the $^{20}\text{Ne} + ^{165}\text{Ho}$ reaction at $E_{\text{lab}} \approx 108.2$ MeV, recorded for 100 s, 20 min after the termination of the irradiation, is shown in Fig. 1. Various peaks observed in the recorded γ -ray spectra were assigned to different ERs, populated in the course of irradiation, on the basis of their characteristic γ -rays as well as by their measured half-lives. The measured half-lives of observed ERs were found to be in good agreement with their literature values taken from Ref. [27]. As a representative case, the half-life decay curve of the ERs ^{179}Os and ^{173}Ta , having half-lives of 6.5 min and 3.14 h, respectively, are shown in Fig. 2.

The reaction cross sections of the observed ERs populated through different fusion processes were calculated using the standard formulation [28], given as

$$\sigma_r = \frac{A\lambda \exp(\lambda t_2)}{N_0\theta\phi\epsilon_G K [1 - \exp(-\lambda t_1)][1 - \exp(-\lambda t_3)]}, \quad (1)$$

where A is the total number of counts recorded under the peak in time t_3 , λ is the decay constant of the product nucleus, N_0

TABLE I. Observed ERs populated through different reaction channels in the $^{20}\text{Ne} + ^{165}\text{Ho}$ reaction at $E_{\text{lab}} \approx 90\text{--}145$ MeV are given in first column along with their half lives in the second column; other columns have spectroscopic properties taken from Ref. [27].

Reaction	Half-life	J^π	E_γ (keV)	I_γ
$^{165}\text{Ho}(^{20}\text{Ne}, 3n)^{182}\text{Ir}$	15.0 min	5^+	126.2	34.4
$^{165}\text{Ho}(^{20}\text{Ne}, p2n)^{182}\text{Os}$	22.1 h	0^+	510.0	52.0
			180.6	33.5
$^{165}\text{Ho}(^{20}\text{Ne}, p3n)^{181}\text{Os}$	105.0 min	$1/2^-$	826.7	20.0
			118.0	12.9
$^{165}\text{Ho}(^{20}\text{Ne}, p5n)^{179}\text{Os}$	6.5 min	$1/2^-$	593.8	94.0
$^{165}\text{Ho}(^{20}\text{Ne}, \alpha)^{181}\text{Re}$	19.9 h	$5/2^+$	365.5	56.0
			639.3	6.4
$^{165}\text{Ho}(^{20}\text{Ne}, \alpha 2n)^{179}\text{Re}$	19.5 min	$5/2^+$	430.2	28.0
			401.7	7.2
$^{165}\text{Ho}(^{20}\text{Ne}, \alpha 3n)^{178}\text{Re}$	13.2 min	3^+	237.3	45.0
			105.3	23.0
			939.1	8.9
$^{165}\text{Ho}(^{20}\text{Ne}, \alpha 4n)^{177}\text{Re}$	14.0 min	$5/2^-$	196.8	8.0
$^{165}\text{Ho}(^{20}\text{Ne}, \alpha p 3n)^{177}\text{W}$	135.0 min	$1/2^-$	115.0	51.0
			376.8	4.6
$^{165}\text{Ho}(^{20}\text{Ne}, \alpha p 4n)^{176}\text{W}$	2.50 h	0^+	99.4	73.0
$^{165}\text{Ho}(^{20}\text{Ne}, 2\alpha 2n)^{175}\text{Ta}$	10.5 h	$7/2^+$	348.5	12.0
$^{165}\text{Ho}(^{20}\text{Ne}, 2\alpha p 3n)^{173}\text{Hf}$	23.6 h	$1/2^-$	296.5	33.9
			139.6	12.7
$^{165}\text{Ho}(^{20}\text{Ne}, 2\alpha 3n)^{174}\text{Ta}$	1.05 h	3^+	206.7	58.0
$^{165}\text{Ho}(^{20}\text{Ne}, 2\alpha 4n)^{173}\text{Ta}$	3.14 h	$5/2^-$	172.2	18.0
			160.4	4.9

is the total number of nuclei present in the target foil, θ is the branching ratio of the identified γ ray, ϕ is the incident beam particle flux, ϵ_G is the geometry-dependent efficiency of the HPGe detector, t_1 is the irradiation time of the stack, t_2 is the time elapsed between the termination of the irradiation and start of the counting, t_3 is the counting time, and $K = [1 - e^{-\mu d}]/\mu d$ is the self-absorption correction factor for the target material of thickness d with absorption coefficient μ . The correction factor for the decay of the induced activity during the termination of the irradiation and beginning of the counting (t_2) is taken as $\exp(\lambda t_2)$ and the correction factor

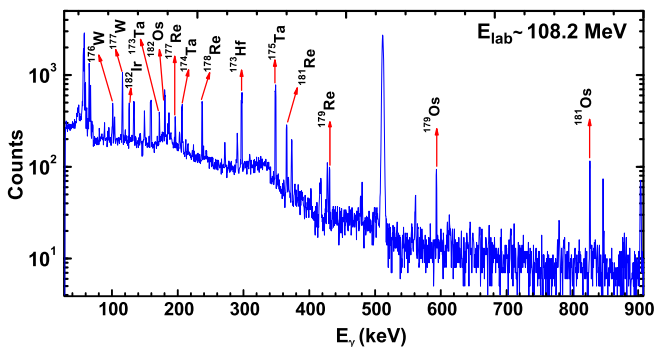


FIG. 1. Typical γ -ray energy spectrum of the evaporation residues populated in the $^{20}\text{Ne} + ^{165}\text{Ho}$ reaction at $E_{\text{lab}} \approx 108.2$ MeV, recorded for 100 s, 20 min after the termination of the irradiation.

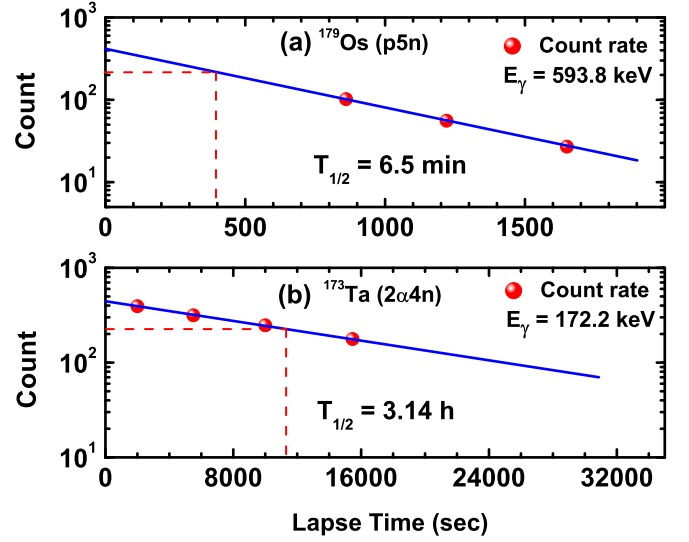


FIG. 2. Half-life decay curve of ERs (a) ^{179}Os (6.5 min) and (b) ^{173}Ta (3.14 h) populated in the $^{20}\text{Ne} + ^{165}\text{Ho}$ reaction at $E_{\text{lab}} \approx 145$ MeV.

due to the decay of the irradiated sample during the data accumulation time t_3 is taken as $1 - \exp(-\lambda t_3)$. During the irradiation, a factor $1 - \exp(-\lambda t_1)$ takes care of the decay of the ERs and is known as the saturation correction factor. Further details regarding the experimental setup and cross section measurement are given in Ref. [29].

Various factors were likely to introduce error and uncertainty in the measured reaction cross sections of the observed ERs. Some of the potential sources of error and uncertainty in the present work are as follows: (i) Fluctuation in the beam current leads to variation in the flux of the incident beam. Proper care was taken to keep the beam current constant. However, error arising due to the fluctuation in beam current was found to be less than 3%. (ii) Nonuniformity in the thickness of the target foil leads to an uncertainty in determining the number of nuclei present in it. In order to check the uniformity of the target foils, the thickness of each target foil was measured at different positions by the α -transmission method. Error contributed due to the uncertainty in thickness of the target foil was found to be less than 3%. (iii) Error arising due to the geometry-dependent detector efficiency, caused by the statistical uncertainty in the counts under the peak, was estimated to be less than 5%. (iv) Error arising due to the dead time of the spectrometer was kept below 10% by suitably adjusting the sample-detector separation. (v) Error associated with the energy straggling of the ion beam was estimated to be less than 2%. Efforts were made to minimize the uncertainty associated with the different sources, and the overall error estimated in the present work does not exceed 15%.

III. ANALYSIS AND INTERPRETATION OF RESULTS

In the $^{20}\text{Ne} + ^{165}\text{Ho}$ reaction at $E_{\text{lab}} \approx 90\text{--}145$ MeV, a total of fourteen ERs, namely ^{182}Ir ($3n$), ^{182}Os ($p2n$), ^{181}Os ($p3n$), ^{179}Os ($p5n$), ^{181}Re (α), ^{179}Re ($\alpha 2n$), ^{178}Re ($\alpha 3n$), ^{177}Re ($\alpha 4n$), ^{177}W ($\alpha p 3n$), ^{176}W ($\alpha p 4n$), ^{175}Ta ($2\alpha 2n$), ^{173}Hf ($2\alpha p 3n$),

^{174}Ta ($2\alpha 3n$), and ^{173}Ta ($2\alpha 4n$) were found to get populated through different fusion processes. Among the observed ERs, residues populated through the α emitting channels (^{181}Re , ^{179}Re , ^{178}Re , ^{177}Re , ^{177}W , ^{176}Re , ^{175}Ta , ^{173}Hf , ^{174}Ta , and ^{173}Ta) have the dual probability of getting populated through the CF process as well as the ICF process. On the other hand, ERs populated through the xn or pxn channels (^{182}Ir , ^{182}Os , ^{181}Os , ^{179}Os) have the possibility of getting populated through the CF process only.

In order to determine the degree of CF and/or ICF contributions in the population of various ERs, measurements of EF of the observed ERs, populated in the $^{20}\text{Ne} + ^{165}\text{Ho}$ reaction, were carried out in the light of well established statistical model code PACE4 [24]. PACE4 is based on the Hauser-Feshbach theory of compound nucleus (CN) decay and uses statistical approach of CN deexcitation by Monte Carlo procedure [30]. The code calculates, at each stage of deexcitation, the angular momentum projection, which enables the determination of angular distribution of the emitted particles. PACE4 uses the Bass model to calculate the fusion cross sections [31]. The optical model potentials of Becchetti and Greenlees [32] are used for calculating the transmission coefficients for neutrons and protons, and the optical model potential of Satchler [33] is used for α -particle emission. In the description of γ -ray competitions, emission of $E1$, $E2$, $M1$, and $M2$ γ -rays are included and the strengths for these transitions are taken from the table of Endt [34]. The decay intensities of these γ rays in Weisskopf units are $E1$: 0.000011; $M1$: 0.01; $E2$: 9.0; and $M2$: 1.2 for the $^{20}\text{Ne} + ^{165}\text{Ho}$ system. The diffuseness parameter (Δ_ℓ) in the transmission coefficient, $T_\ell = [1 + \exp(\frac{\ell - \ell_{\text{max}}}{\Delta_\ell})]^{-1}$, is taken as $4\hbar$, and the value of the fusion barrier, from PACE4 calculations for the entire energy range, was found to be 80.48 MeV. In the statistical model code PACE4 three important parameters were used for determining the various level densities needed for calculations. These are the ‘‘little- a ’’ parameter (involved in the particle evaporation calculation), the ratio a_f/a (of the little- a parameter at the saddle point and ground state deformations), and B_f , the fission barrier (which is taken to be equal to the rotating liquid drop fission barrier). The little- a parameter, which influences the equilibrium state components of the cross section, is given as $a = A/K$, where A is the mass number of the compound nucleus and K is an adjustable parameter, which may be varied to match the experimental data. Kataria *et al.* [35], on the basis of results of earlier investigations on thermodynamic properties of the nuclei, presented a semiempirical nuclear level density formula. In the present work, the value of K in PACE4 calculation is taken according to the prescription of Kataria *et al.* [35]. It is to be noted that any enhancement in the experimentally measured EF over the PACE4 prediction may be attributed to some physical phenomenon not incorporated in the PACE4 calculation.

A. Evaporation residues populated through the xn and pxn channels

In the $^{20}\text{Ne} + ^{165}\text{Ho}$ reaction at $E_{\text{lab}} \approx 90\text{--}145$ MeV, a total of four residues, namely ^{182}Ir , ^{182}Os , ^{181}Os , and ^{179}Os , were

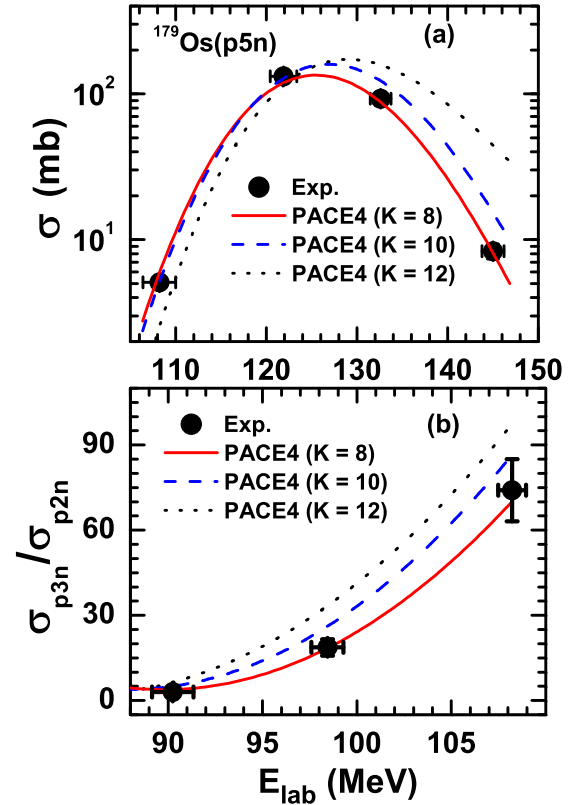


FIG. 3. Experimentally measured and PACE4 calculated (a) EF of the ER ^{179}Os populated through the $p5n$ channel and (b) ratio of σ_{p3n} to σ_{p2n} as a function of E_{lab} .

found to get populated through the xn ($x = 3$) and pxn ($x = 2, 3, 5$) channels. Fusion of the ^{20}Ne projectile with the ^{165}Ho target as a single entity leads to the formation of an excited intermediate compound system $^{185}\text{Ir}^*$, incorporating the total momentum and energy of the incident projectile. The excited intermediate compound system $^{185}\text{Ir}^*$ further decays via the emission of nucleons and γ -rays leading to the formation of the ERs ^{182}Ir , ^{182}Os , ^{181}Os , and ^{179}Os through the $3n$, $p2n$, $p3n$, and $p5n$ channels, respectively. As a representative case, formation of the ER ^{179}Os through the $p5n$ channel may be given as

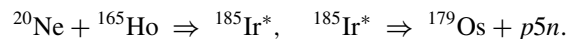


Figure 3(a) shows the experimentally measured and PACE4 calculated EF of the ER ^{179}Os populated through the $p5n$ channel. The experimentally measured and PACE4 calculated ratio of σ_{p3n} to σ_{p2n} as a function of E_{lab} is shown in Fig. 3(b). In order to reproduce the experimentally measured EFs of ERs populated through the xn and pxn channels in the $^{20}\text{Ne} + ^{165}\text{Ho}$ reaction at $E_{\text{lab}} \approx 90\text{--}145$ MeV, the level density parameter (K) in the statistical model code PACE4 was varied from 8 to 12 in steps of 2 (i.e., $K = 8, 10, 12$) according to the prescription of Kataria *et al.* [35] and Fabris *et al.* [36]. As can be inferred from Fig. 3, the experimentally measured excitation function of the ER ^{179}Os and the ratio of σ_{p3n} to σ_{p2n} were well reproduced by the statistical model code PACE4 for level density parameter $K = 8$. Similarly, the experimentally

measured EFs of the ERs ^{182}Ir , ^{182}Os , and ^{181}Os populated through the $3n$, $p2n$, and $p3n$ channels, respectively, were also well reproduced by the code PACE4 for $K = 8$, emphasizing their formation through the CF process only.

B. Evaporation residues populated through the α emitting channels

As pointed out in the beginning of Sec. III, ERs emerging through the α emitting channels have the dual probability of getting populated through the CF process as well as the ICF process. In the $^{20}\text{Ne} + ^{165}\text{Ho}$ reaction at $E_{\text{lab}} \approx 90\text{--}145$ MeV, a total of ten ERs, namely ^{181}Re , ^{179}Re , ^{178}Re , ^{177}Re , ^{177}W , ^{176}Re , ^{175}Ta , ^{173}Hf , ^{174}Ta , and ^{173}Ta , were found to get populated through the α emitting channels. The low $E_{\text{B.U.}}$ value of the incident projectile (^{20}Ne) makes it susceptible to the breakup fusion or ICF reaction, in which the incident projectile breaks up into fragments prior to fusion with the target nucleus. ^{20}Ne is expected to break up into 1α ($^{16}\text{O} + \alpha$) or 2α [$^{12}\text{C} + 2\alpha$ (^8Be)] fragments in the periphery of the target nucleus owing to its low $E_{\text{B.U.}}$ value, and the resulting breakup fragments ^{16}O and ^{12}C further fuse with the ^{165}Ho target leading to the formation of the incompletely fused compound systems $^{181}\text{Re}^*$ and $^{177}\text{Ta}^*$ through the ICF^α and $\text{ICF}^{2\alpha}$ processes, respectively. Thus, ERs populated through the α emitting channels have varying degree of contributions arising from the ICF^α , $\text{ICF}^{2\alpha}$, and CF processes.

Figure 4 shows the EF of the ER ^{174}Ta populated through the $2\alpha 3n$ channel. As can be seen, the experimentally measured EF of the ER ^{174}Ta shows an enhancement over the PACE4 prediction for the entire energy range. ER ^{174}Ta was found to get populated through the 2α emitting channel and is likely to have contributions arising from the CF, ICF^α , as well as $\text{ICF}^{2\alpha}$ processes. Since the PACE4 calculations takes into account only the CF process and do not incorporate the contribution arising from the ICF processes, the observed enhancement in the experimentally measured EF over the PACE4 prediction may be attributed to the contributions arising from the ICF^α and $\text{ICF}^{2\alpha}$ processes. Similarly, the experimentally measured EF of the ERs ^{181}Re , ^{179}Re , ^{178}Re , ^{177}Re , ^{177}W , ^{176}Re , ^{175}Ta , ^{173}Hf , and ^{173}Ta populated through α and/or 2α emitting channels also shows an enhancement over the PACE4 prediction, suggesting the presence of ICF processes in addition to CF process in their evolution. Tables II and III gives the experimentally measured reaction cross section of the observed ERs populated through xn , pxn , and/or α

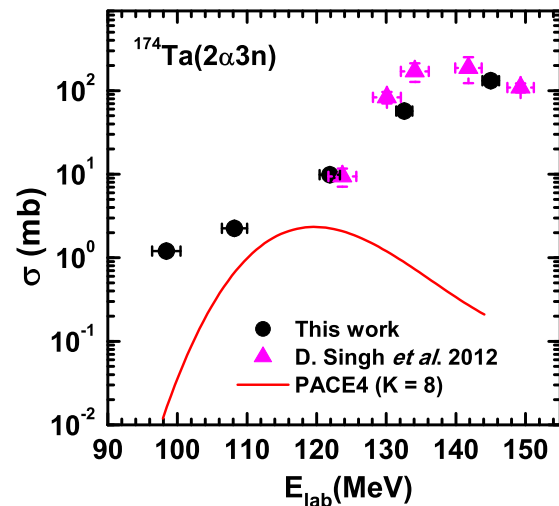


FIG. 4. Experimentally measured and PACE4 calculated EF of the ER ^{174}Ta populated through the $2\alpha 3n$ channel. Solid (black) circles are the results of the present work and solid (pink) triangles represent the work of Singh *et al.* [23].

emitting channels in the $^{20}\text{Ne} + ^{165}\text{Ho}$ reaction at $E_{\text{lab}} \approx 90\text{--}145$ MeV.

C. Critical angular momentum: Limiting the complete fusion

Formation of a compound nucleus through CF and/or ICF processes is likely to be governed by the quantum of angular momentum associated with the incident projectile. So far various studies on ICF reactions have already been carried out, and based on their results several models were also proposed. However, the mechanism involved in the ICF process is still only partially understood, especially in terms of the angular momentum involved in the population of ERs. It was suggested by Trautmann *et al.* [37] that ICF reactions arise mainly through peripheral collisions between the incident projectile and target. On the other hand, Tricoire *et al.* [38] observed that, in the case of fusion reactions involving spherical targets, the ICF processes were dominant reaction modes even at lower angular momentum. Experimentally it is now well established that, for HI induced reactions, the contribution of the CF cross section towards the TF cross section decreases at energies well above the Coulomb barrier while the TF cross section continues to increase. This

TABLE II. Experimentally measured reaction cross sections of the observed ERs populated in the $^{20}\text{Ne} + ^{165}\text{Ho}$ reaction at $E_{\text{lab}} \approx 90\text{--}145$ MeV.

E_{lab} (MeV)	^{182}Ir (mb)	^{182}Os (mb)	^{181}Os (mb)	^{179}Os (mb)	^{181}Re (mb)	^{179}Re (mb)	^{178}Re (mb)
90.2 ± 2.1	0.5 ± 0.11	0.35 ± 0.02	1.15 ± 0.1		0.45 ± 0.03	0.9 ± 0.02	8.0 ± 0.7
98.4 ± 2.0	1.2 ± 0.15	0.8 ± 0.08	15.1 ± 1.8		1.31 ± 0.15	1.4 ± 0.15	32.2 ± 3.1
108.2 ± 1.8	0.3 ± 0.03	0.1 ± 0.01	7.4 ± 0.8	5.1 ± 0.4	12.2 ± 1.1	12.6 ± 1.2	26.9 ± 2.1
121.9 ± 1.4			0.19 ± 0.02	131.9 ± 11.5	24.7 ± 2.2	73.4 ± 7.9	62.1 ± 6.2
132.6 ± 1.1				92.5 ± 9.1	12.5 ± 1.1	132.5 ± 12.5	51.6 ± 5.1
145.0 ± 1.2				8.3 ± 0.9	4.8 ± 0.3	124.3 ± 10.2	52.4 ± 4.8

TABLE III. Experimentally measured reaction cross sections of the observed ERs populated in the $^{20}\text{Ne} + ^{165}\text{Ho}$ reaction at $E_{\text{lab}} \approx 90\text{--}145$ MeV.

E_{lab} (MeV)	^{177}Re (mb)	^{177}W (mb)	^{176}W (mb)	^{175}Ta (mb)	^{173}Hf (mb)	^{174}Ta (mb)	^{173}Ta (mb)
90.2 ± 2.1	10.6 ± 1.1	1.6 ± 0.1	0.2 ± 0.02				
98.4 ± 2.0	31.2 ± 2.9	3.2 ± 0.4	0.6 ± 0.05	2.1 ± 0.2		1.2 ± 0.1	
108.2 ± 1.8	85.6 ± 8.4	10.2 ± 1.1	5.5 ± 0.5	5.2 ± 0.5		2.2 ± 0.1	2.7 ± 0.3
121.9 ± 1.4	87.0 ± 7.6	84.5 ± 8.1	51.8 ± 5.1	27.3 ± 2.1	2.2 ± 0.2	9.8 ± 0.8	5.4 ± 0.5
132.6 ± 1.1	156.7 ± 15.2	52.3 ± 4.8	119.2 ± 10.1		4.2 ± 0.4	57.2 ± 5.2	10.5 ± 1.1
145.0 ± 1.2	145.8 ± 14.2	71.2 ± 6.2	131.5 ± 12.5		11.6 ± 1.1	131.2 ± 12.3	13.6 ± 1.3

systematic behavior of the CF and TF cross sections at energies above the barrier was considered by many authors to be a consequence of the critical angular momentum associated with the compound system [39,40]. In order to explore the role of the input angular momentum in the formation of compound nucleus through CF and/or ICF processes, the sum-rule model was proposed by Siwek-Wilczynska *et al.* [41]. According to the sum-rule model, ICF reactions are localized in the angular momentum space above the limiting value, called critical angular momentum ℓ_{crit} . For $\ell > \ell_{\text{crit}}$, the attractive pocket in the effective potential vanishes and hence the interacting system cannot proceed via the CF process. In order to shed the excess angular momentum, the incident projectile fuses with the target nucleus through the ICF process. At low incident energy, the maximum angular momentum (ℓ_{max}) associated with the interacting system is close to the ℓ_{crit} value, thereby precluding any space for the ICF reactions above ℓ_{crit} .

Based on the liquid drop model, Wilczynski [42] suggested that ℓ_{crit} can be well approximated by the equilibrium condition of the nuclear, Coulomb, and centrifugal forces as

$$2\pi(\gamma_1 + \gamma_2) \frac{R_1 R_2}{R_1 + R_2} = \frac{Z_1 Z_2 e^2}{(R_1 + R_2)^2} + \frac{\ell_{\text{crit}}(\ell_{\text{crit}} + 1)\hbar^2}{\mu(R_1 + R_2)^3}, \quad (2)$$

where μ is the reduced mass of the projectile-target system and R_1, R_2 are taken as half-density radii corresponding to the maximum attraction between the projectile and the target. Surface tension coefficients γ_i were taken in the form

$$\gamma_i = 0.99 \left\{ 1 - 1.78 \left(\frac{N_i - Z_i}{A_i} \right)^2 \right\} \text{MeV fm}^{-2}. \quad (3)$$

For the incident energy at which ℓ_{crit} is below the maximum possible angular momentum associated with the system ℓ_{max} , the CF cross section may be given as

$$\sigma_{\text{CF}} = \pi \lambda^2 \sum_{\ell=0}^{\ell_{\text{crit}}} (2\ell + 1) T_{\ell}, \quad (4)$$

where λ is the reduced wavelength ($\lambda^2 = \frac{\hbar^2}{2\mu E_{\text{c.m.}}}$) and T_{ℓ} is the transmission coefficient for incident angular momentum ℓ . According to sharp cutoff approximation proposed by Wilczynski [42], transmission coefficient T_{ℓ} may be taken as

$$T_{\ell} = \begin{cases} 1 & \text{for } \ell \leq \ell_{\text{max}}, \\ 0 & \text{for } \ell > \ell_{\text{max}}, \end{cases}$$

where ℓ_{max} corresponds to the peripheral collision and is given by

$$\ell_{\text{max}} = R \sqrt{2\mu(E_{\text{c.m.}} - V_B)/\hbar^2}. \quad (5)$$

Here R is the maximum distance between the two nuclei at which the collision leads to a reaction and V_B is the fusion barrier of the system at a distance R .

In order to extract the value of ℓ_{crit} at each incident energy using Eq. (4), the value of σ_{CF} is required. In the present work, the offline γ -ray detection method was used to identify the various ERs populated in the course of irradiation. One of the major drawbacks of the offline technique is that ERs with too short or long half lives could not be detected due to the lapse time of the experiment. In order to incorporate the cross section of the missing stable and unstable ERs into the total CF cross section, statistical model code PACE4 was used. Using the code PACE4, the ratio $R = \sum \sigma_{xn+pxn}^{\text{PACE4}} / \sigma_{\text{fus}}^{\text{PACE4}}$ was calculated, and using this ratio the experimental CF cross section was calculated as $\sigma_{\text{CF}}^{\text{exp}} = \sum \sigma_{xn+pxn}^{\text{exp}} / R$ [43]. Here, $\sigma_{\text{fus}}^{\text{PACE4}}$ is the PACE4 calculated total CF cross section which includes the contribution arising from ERs populated through the xn , pxn , and α emitting channels. Thus, $\sigma_{\text{CF}}^{\text{exp}}$ is the corrected total experimental CF cross section, having contributions from all the CF channels, observed as well as missing. Table IV gives the value of $\sigma_{\text{CF}}^{\text{exp}}$ and the extracted value of ℓ_{crit} from $\sigma_{\text{CF}}^{\text{exp}}$ data at each incident energy for the $^{20}\text{Ne} + ^{165}\text{Ho}$ system. The fourth column of Table IV gives the value of ℓ_{crit} calculated using the code CCFULL [25]. As can be observed from Table IV, the values of ℓ_{crit} extracted

TABLE IV. Experimental fusion cross section ($\sigma_{\text{CF}}^{\text{exp}}$) along with ℓ_{crit} (fusion) derived from the $\sigma_{\text{CF}}^{\text{exp}}$ data, ℓ_{crit} (CCFULL) calculated using the code CCFULL [25], and ℓ_{max} for the $^{20}\text{Ne} + ^{165}\text{Ho}$ system at different E_{lab} ($E_{\text{c.m.}}$) and the corresponding excitation energy (E^*) (see text for details).

E_{lab} ($E_{\text{c.m.}}$) (MeV)	E^* (MeV)	$\sigma_{\text{CF}}^{\text{exp}}$ (mb)	ℓ_{crit} (fusion) (\hbar)	ℓ_{crit} (CCFULL) (\hbar)	ℓ_{max} (\hbar)
90.2 (80.4)	48.8	15.4	5	7	8
98.4 (87.7)	56.1	194.3	21	25	28
108.2 (96.5)	64.9	412.1	32	30	41
121.9 (108.7)	77.1	684.4	44	44	55
132.6 (118.2)	86.6	880.9	53	53	63
145.0 (129.3)	97.7	967.4	58	60	72

TABLE V. List of reactions studied in this work. The first and last columns denote the projectile and target of the reaction. The second column represents the breakup threshold energy ($E_{B.U.}$) of the projectile.

Projectile	$E_{B.U.}$ (MeV)	Target		
^{12}C	7.36	^{89}Y [43]		
		^{93}Nb [44]		
		^{115}In [60]		
		^{159}Tb [5]		
		^{165}Ho [45]		
		^{181}Ta [46]		
		^{16}O	7.16	^{49}Sc [57]
				^{51}V [47]
				^{89}Y [1]
				^{103}Rh [48]
^{115}In [3]				
^{130}Te [58]				
^{20}Ne	4.73	^{159}Tb [49]		
		^{165}Ho [4]		
		^{169}Tm [59]		
		^{181}Ta [50]		
		^{51}V [2]		
		^{55}Mn [16]		
		^{59}Co [21]		
		^{159}Tb [22]		
		^{165}Ho (present work)		
		^{169}Tm [22]		

from the fusion cross section data are in good agreement with the values calculated using the code CCFULL. Moreover, the values of l_{crit} extracted from the CF cross sections as well as those calculated using the code CCFULL were found to lie sufficiently below the hard grazing value l_{max} , the maximum angular momentum corresponding to a given incident energy, approximated using Eq. (5). Thus, it can be said that in the present work the ICF reactions originate mainly through peripheral collisions, involving the partial waves localized in the l space between the l_{crit} and l_{max} .

The sum-rule model was further used to investigate the role of the incident projectile in deciding the magnitude of the limiting angular momentum l_{crit} . According to sum-rule model [Eq. (2)], the value of l_{crit} for a given system is govern by the static properties, viz., size and mass of the interacting system. In order to study the systematic of l_{crit} and its dependence on projectile and target structure, the values of l_{crit} for the ^{20}Ne , ^{16}O , and ^{12}C induced reactions with different targets were calculated using the sum-rule model and are shown in Fig. 5 (solid curves) as a function of Z of the fusing system, i.e., $Z = Z_p + Z_T$. Also shown in Fig. 5 are the values of l_{crit} extracted from the experimentally measured CF cross sections [using Eq. (4)] at the excitation energy of 77 MeV for the various systems listed in Table V. ^{20}Ne , ^{16}O , and ^{12}C projectiles differ significantly from each other in terms of their $E_{B.U.}$ values as well as their structures. ^{20}Ne , ^{16}O , and ^{12}C are α cluster projectiles having 5α , 4α , and 3α cluster structure with $E_{B.U.}$ values of 4.73, 7.16, and 7.37 MeV, respectively. As can be

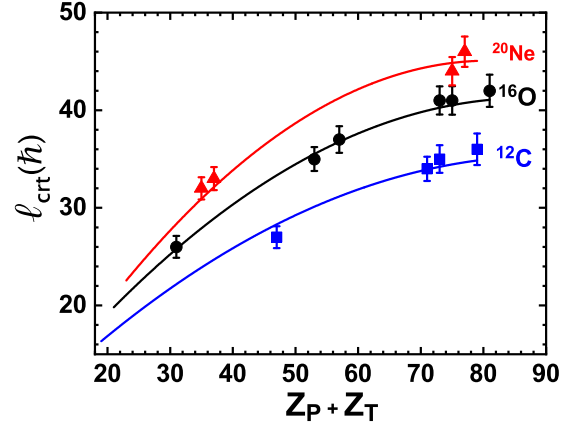


FIG. 5. Critical angular momentum (l_{crit}) derived from the fusion cross section for the ^{12}C (solid square), ^{16}O (solid circle), and ^{20}Ne (solid triangle) induced reactions as a function of Z of the compound system at $E^* = 77$ MeV. Solid lines represents the prediction of the sum-rule model [41]. See text for details.

seen from Fig. 5, the value of l_{crit} increases gradually with the target charge for a given incident projectile. Moreover, the value of l_{crit} was also found to depend on the $E_{B.U.}$ value of the incident projectile. For a given target, higher the $E_{B.U.}$ value of the incident projectile, lower is the corresponding l_{crit} value of the system.

D. ICF probability: Driven by entrance channel parameters

In order to investigate the role of various entrance channel parameters on fusion incompleteness, coupled channels (CC) calculations were performed using a modified version of the code CCFULL [25] for the $^{20}\text{Ne} + ^{165}\text{Ho}$ system. CC calculations performed using the code CCFULL do not take into account the coupling to unbound or continuum states and hence the breakup of the incident projectile is not taken into account. In the CCFULL calculations, the values of the nuclear potential depth V_0 , radius parameter r_0 , and diffuseness parameter a were obtained using the Wood-Saxon parametrization of the Akyuz-Winther (AW) potential [51] to reproduce the fusion barrier, $V_b = 80.48$ MeV (Bass fusion barrier) taken from the PACE4 calculation. The values of V_0 , r_0 , and a for the present CCFULL calculations were taken as 85.0 MeV, 1.14 fm, and 0.64 fm, respectively, which were found to lie very close to the values calculated using the Wood-Saxon parametrization of the AW potential.

The result of CC calculations performed using the code CCFULL for the $^{20}\text{Ne} + ^{165}\text{Ho}$ system is shown in Fig. 6. As can be inferred from Fig. 6, the fusion cross sections obtained from the CC calculations (shown by the solid line) are relatively higher than the experimentally measured CF cross sections (solid circles) at energies above the barrier. In order to reproduce the experimentally measured CF cross sections, CC calculations were multiplied by a factor of 0.74, shown by the dashed line in Fig. 6. Thus, it can be concluded that experimentally measured CF cross sections for the $^{20}\text{Ne} + ^{165}\text{Ho}$ system were suppressed by 26% in comparison to values predicted by the CC calculations performed using the code CCFULL.

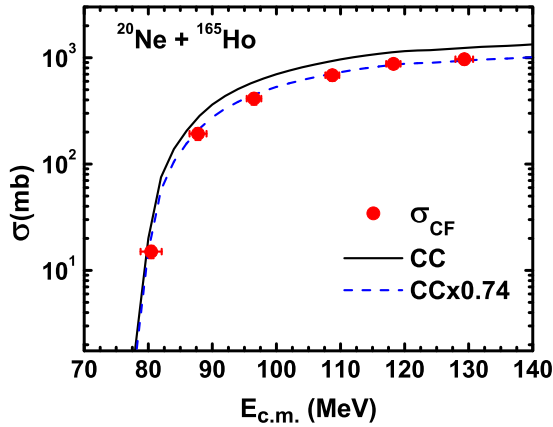


FIG. 6. Experimentally measured CF excitation function (solid circle) along with the coupled channels calculations (solid line) performed using the code CCFULL. The dashed line shows the coupled channels calculations scaled down by a factor of 0.74.

In order to further confirm the role of the breakup fusion reaction in influencing the degree of fusion incompleteness, dimensionless physical quantities, fusion function $F(x)$ and x , were formulated as

$$F(x) = \frac{2E_{c.m.}}{R_b^2 \hbar \omega} \sigma_{CF}, \quad x = \frac{E_{c.m.} - V_b}{\hbar \omega}, \quad (6)$$

using the CF cross section, as suggested by Canto *et al.* [20]. Barrier parameters R_b , V_b , and $\hbar \omega$ used in the formulation of $F(x)$ and x were taken from the CC calculations performed using the code CCFULL.

Reduction of the experimentally measured CF cross section to the fusion function is derived from the Wong formula [52]. On simplifying the Wong formula, $F(x)$ reduces to

$$F_0(x) = \ln[1 + \exp(2\pi x)], \quad (7)$$

which is known as the universal fusion function (UFF). Formulation of the fusion function $F(x)$ takes care of the static effect of the interacting nuclei, and inelastic and transfer coupling are not so effective at energies above the barrier. Thus, any deviation of the CF function from the UFF may be attributed to the effect of projectile breakup on CF cross section. Figure 7 shows the variation of CF function $F(x)$ with x (solid circles) for the $^{20}\text{Ne} + ^{165}\text{Ho}$ system. For the ^{20}Ne projectile the most favorable breakup channel is $^{20}\text{Ne} \Rightarrow ^{16}\text{O} + \alpha$, owing to its low $E_{B,U.}$ value of 4.73 MeV. It can be observed from Fig. 7 that the fusion functions derived from the experimentally measured CF cross sections were suppressed with respect to the UFF (solid line). When the UFF is scaled down by a factor of 0.74 (dashed line) it shows satisfactory overlap with the CF functions. Thus, it can be concluded from the UFF calculation that experimentally measured CF functions for the $^{20}\text{Ne} + ^{165}\text{Ho}$ system were suppressed by 26% with respect to UFF due to breakup of the incident projectile in the vicinity of the target nucleus.

The degree of ICF probability (P_{ICF}), given as $P_{ICF} = \frac{\sigma_{ICF}}{\sigma_{CF} + \sigma_{ICF}}$, or equivalently the suppression in fusion cross section with respect to CC or one-dimension barrier penetration model (1DBPM) calculations, was found to

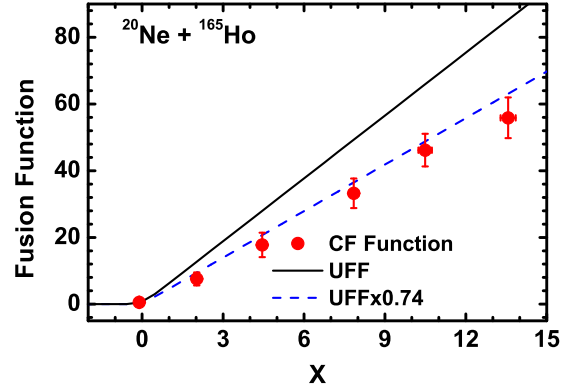


FIG. 7. Experimentally measured CF function $F(x)$ for the $^{20}\text{Ne} + ^{165}\text{Ho}$ system (solid circle) along with the UFF (solid line). The dashed line shows the UFF scaled down by a factor of 0.74.

depend on various entrance channel parameters, particularly on mass asymmetry ($\frac{A_T}{A_T + A_P}$) of the projectile-target system and Coulomb repulsion. The dependence of P_{ICF} on mass asymmetry of the projectile-target system was first pointed out by Morgenstern *et al.* [53]. Morgenstern *et al.* suggested that the colliding nuclei approach each other with a relative velocity V_{rel} given as

$$V_{rel} = \sqrt{\frac{2(E_{c.m.} - V_B)}{\mu}}, \quad (8)$$

and come to rest in the center-of-mass frame after fusion. Here, μ is the reduced mass of the interacting system and V_B is the fusion barrier. Morgenstern *et al.* concluded that at a given V_{rel} the ICF fraction increases with increase in mass asymmetry of the projectile-target system. In order to test the consistency of the Morgenstern *et al.* mass asymmetry effect, the ICF fraction or probability was estimated by comparing the experimentally measured fusion cross section data with the CC or 1DBPM calculations performed using the code CCFULL for the ^{20}Ne induced reaction with different targets. Fig. 8 shows the variation of ICF fraction as a function of mass asymmetry and Coulomb repulsion ($Z_P Z_T$) for the ^{20}Ne induced reaction with various targets. It can be inferred from Fig. 8 that ICF probability (P_{ICF}) depends strongly on mass asymmetry as well as on Coulomb repulsion between the interacting system and increases with increase in entrance channel parameters.

So far several studies on fusion reaction have been carried out involving loosely as well as tightly bound projectiles. The results of these works were insufficient in establishing a systematic of fusion suppression and its dependency on target charge (Z_T). It is speculated that as Z_T decreases, the dominance of Coulomb breakup becomes weaker and subsequently the ICF probability decreases. In order to explore the role of Coulomb repulsion on fusion suppression, a detailed study of angular distribution of single and coincident α particles emerging from the $^9\text{Be} + ^{208}\text{Pb}$ reaction was carried out by Hinde *et al.* [54]. On the basis of their work, Hinde *et al.* proposed an empirical formula for the prediction of P_{ICF} . Applying the same empirical formula to the present system, the

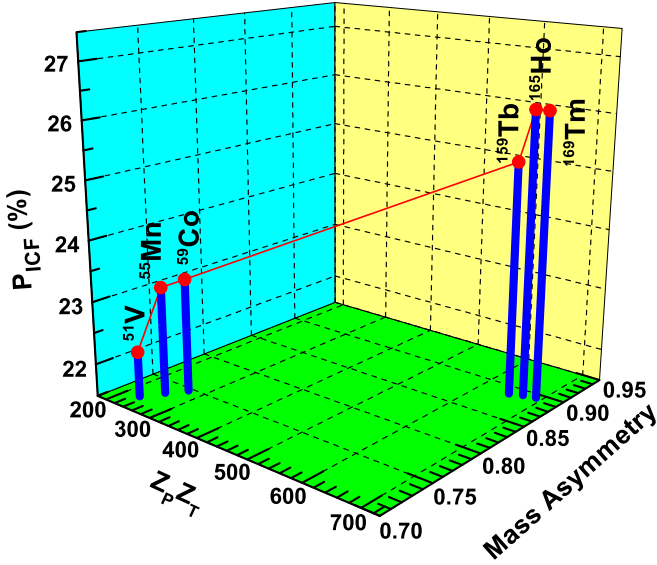


FIG. 8. Incomplete fusion probability (P_{ICF}) as a function of Coulomb repulsion ($Z_p Z_T$) and mass asymmetry [$A_p/(A_p + A_T)$] for the ^{20}Ne induced reaction with ^{51}V [2], ^{55}Mn [16], ^{59}Co [21], ^{159}Tb [22], ^{165}Ho (this work), and ^{169}Tm [22] targets.

P_{ICF} of 26% observed in the $^{20}\text{Ne} + ^{165}\text{Ho}$ system is scaled to predict the P_{ICF} for ^{20}Ne induced reactions with any target as

$$P_{ICF} = P_{ICF}(^{165}\text{Ho}) \frac{V'_N}{V'_N(^{165}\text{Ho})} \times \exp\{-0.924[R_s - R_s(^{165}\text{Ho})]\}. \quad (9)$$

All the quantities in the above equation were evaluated at the proper fusion barrier radius R_B calculated using the Sao Paulo potential [55]. The nuclear potentials for the ^{20}Ne induced reaction with different targets were calculated using the empirical formula prescribed by Christensen and Winther [56] as

$$V'_N = -50 \frac{R_p R_T}{R_p + R_T} \exp\left(\frac{-R_s}{0.63}\right), \quad (10)$$

where R_p , R_T , and R_s are the projectile radius, target radius, and surface-to-surface separation, respectively. The value of R_s is approximated as $R_s = R_B - R(^{20}\text{Ne}) - R_T$. Similarly, the P_{ICF} of 18% and 15% observed in the case of ^{16}O [4] and ^{12}C [45] induced reactions, respectively, with the ^{165}Ho target were also scaled to predict the ICF probability for the ^{16}O and ^{12}C induced reactions with other targets listed in Table V. Figure 9 shows the variation of P_{ICF} as a function of Z_T for the ^{20}Ne , ^{16}O , and ^{12}C induced reactions. Solid lines (red, black, and blue) in Fig. 9 correspond to the predictions of the empirical formula, given by Hinde *et al.* [54], for the ^{20}Ne , ^{16}O , and ^{12}C induced reactions, respectively. As can be observed from Fig. 9, the P_{ICF} for different projectiles increase monotonically with Z_T , justifying the major role played by the Coulomb repulsion in the breakup of the incident projectile in the vicinity of the target nucleus. Also it is quite evident from Fig. 9 that $E_{B,U.}$ of the incident projectile plays a vital role in influencing the P_{ICF} . ^{20}Ne is the most loosely bound α cluster projectile among ^{20}Ne , ^{16}O , and ^{12}C , having an $E_{B,U.}$ value of 4.73 MeV,

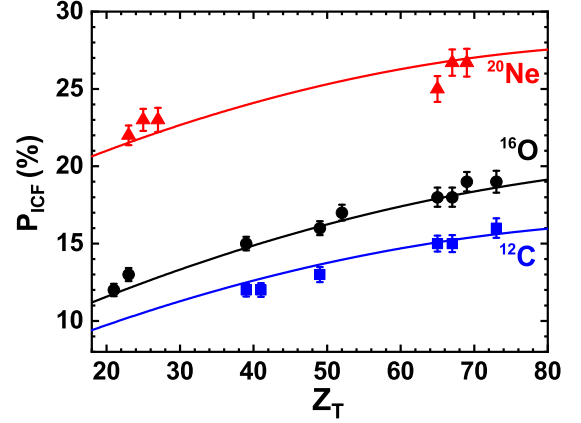


FIG. 9. Incomplete fusion probability (P_{ICF}) for the ^{12}C (solid square), ^{16}O (solid circle), and ^{20}Ne (solid triangle) induced reactions as a function of Z of the target nuclei. Solid lines represent the prediction of the empirical formula given by Hinde *et al.* [54] for the respective projectiles. See text for details.

whereas ^{16}O and ^{12}C have $E_{B,U.}$ values of 7.16 and 7.37 MeV, respectively. This hierarchy of $E_{B,U.}$ values is reflected clearly in the P_{ICF} of ^{20}Ne , ^{16}O , and ^{12}C induced reactions. The P_{ICF} for ^{20}Ne induced reactions lies above the ^{16}O induced reactions which in turn lies above the ^{12}C induced reactions.

IV. CONCLUSION

In order to investigate the degree of ICF contribution and its dependence on various entrance channel parameters, measurements of EF of the observed ERs populated in the $^{20}\text{Ne} + ^{165}\text{Ho}$ reaction at $E_{\text{lab}} \approx 90\text{--}145$ MeV have been carried out. EFs of the ERs populated through xn/pxn channels were well reproduced by the statistical model code PACE4, corroborating their evolution through the CF process. On the other hand, EFs of the ERs populated through the α emitting channels show an enhancement over the PACE4 predictions, probably arising due to the presence of ICF processes in addition to the CF process in their population. Experimentally measured total CF cross sections were found to be suppressed by 26% with respect to CC calculations performed using the code CCFULL. The same degree of suppression was also observed when extracted CF functions were compared with the UFF. The observed ICF fraction or probability, estimated by the degree of fusion suppression with respect to CC calculations, was found to strongly depend on two dominant entrance channel parameters, namely mass asymmetry and Coulomb repulsion. The role of Coulomb repulsion on fusion probability was further explored by comparing the P_{ICF} of ^{20}Ne , ^{16}O , and ^{12}C induced reactions with different targets using the empirical formula given by Hinde *et al.* [54]. It was observed that P_{ICF} for ^{20}Ne , ^{16}O , and ^{12}C induced reactions were in good agreement with the empirical predictions made by Hinde *et al.* and increase monotonically with the increase in target charge (Z_T), pointing out a major role played by the Coulomb repulsion in the breakup fusion reaction. Moreover, the role of the $E_{B,U.}$ value of the incident projectile was also reflected

from the systematics of P_{ICF} for the fusion reactions induced by different α cluster projectiles.

ACKNOWLEDGMENTS

S.A. is thankful to Principal MANUU Polytechnic Darbhanga, Chairman Department of Physics AMU Aligarh, and

Director VECC Kolkata for providing the necessary facilities to carry out this work and Dr. Md. Moin Shaikh (Research Associate, VECC Kolkata) for fruitful discussion and suggestions. S.A. is also thankful to MANUU Hyderabad and University Grants Commission New Delhi for providing the financial support in the form of a Minor Research Project grant (MANUU/Acad/F.404/2016-17/217).

-
- [1] M. Gull *et al.*, *Phys. Rev. C* **98**, 034603 (2018).
 [2] S. Ali *et al.*, *Eur. Phys. J. A* **54**, 56 (2018).
 [3] K. Kumar *et al.*, *Phys. Rev. C* **88**, 064613 (2013).
 [4] K. Kumar *et al.*, *Phys. Rev. C* **87**, 044608 (2013).
 [5] A. Yadav *et al.*, *Phys. Rev. C* **85**, 034614 (2012).
 [6] J. M. Alexander and D. H. Sisson, *Phys. Rev.* **128**, 2288 (1962).
 [7] Marshall and A. Ewart, *Phys. Rev.* **134**, B783 (1964).
 [8] H. C. Britt and A. R. Quinton, *Phys. Rev.* **124**, 877 (1961).
 [9] A. Yadav *et al.*, *Phys. Rev. C* **85**, 064617 (2012).
 [10] B. S. Tomar, A. Goswami, A. V. R. Reddy, S. K. Das, P. P. Burte, S. B. Manohar, and B. John, *Phys. Rev. C* **49**, 941 (1994).
 [11] Md. M. Shaikh *et al.*, *Phys. Rev. C* **93**, 044616 (2016); and the references therein.
 [12] Mohd. Shuaib *et al.*, *Phys. Rev. C* **94**, 014613 (2016).
 [13] T. Inamura *et al.*, *Phys. Lett. B* **68**, 51 (1977).
 [14] S. Ali *et al.*, *J. Mod. Phys.* **5**, 2063 (2014).
 [15] A. Yadav *et al.*, *Phys. Rev. C* **86**, 014603 (2012).
 [16] R. Ali *et al.*, *J. Phys. G: Nucl. Part. Phys.* **37**, 115101 (2010).
 [17] H. Kumar *et al.*, *Eur. Phys. J. A* **54**, 47 (2018).
 [18] H. E. Martz *et al.*, *Nucl. Phys. A* **439**, 299 (1985), and the references therein.
 [19] D. J. Parker, J. Asher, T. W. Conlon, and I. Naqib, *Phys. Rev. C* **30**, 143 (1984).
 [20] L. F. Canto *et al.*, *Nucl. Phys. A* **821**, 51 (2009).
 [21] D. Singh, R. Ali, M. Afzal Ansari, B. S. Tomar, M. H. Rashid, R. Guin, and S. K. Das, *Phys. Rev. C* **83**, 054604 (2011).
 [22] J. Cabrera *et al.*, *Phys. Rev. C* **68**, 034613 (2003).
 [23] D. Singh *et al.*, *Nucl. Phys. A* **879**, 107 (2012).
 [24] O. B. Tarasov and D. Bazin, *Nucl. Instrum. Methods Phys. Res., Sect. B* **266**, 4657 (2008); A. Gavron, *Phys. Rev. C* **21**, 230 (1980).
 [25] K. Hagino *et al.*, *Comput. Phys. Commun.* **123**, 143 (1999).
 [26] J. F. Ziegler, SRIM-2006, The Stopping Power and Range of Ions in Matter, <http://www.srim.org/SRIM/SRIMLEGL.htm>
 [27] National Nuclear Data Center, Brookhaven National Laboratory, <https://www.nndc.bnl.gov/chart>
 [28] I. A. Rizvi *et al.*, *Indian J. Phys.* **86**, 913 (2012); and the references therein.
 [29] F. K. Amanuel *et al.*, *Eur. Phys. J. A* **47**, 156 (2011).
 [30] H. Feshbach and V. F. Weisskope, *Phys. Rev.* **76**, 1550 (1949).
 [31] R. Bass, *Nucl. Phys. A* **231**, 45 (1974).
 [32] F. D. Becchetti and G. W. Greenlees, *Phys. Rev.* **182**, 1190 (1969).
 [33] G. R. Satchler, *Nucl. Phys.* **70**, 177 (1965).
 [34] P. M. Endt, *At. Data Nucl. Data Tables* **26**, 47 (1981).
 [35] S. K. Kataria, V. S. Ramamurthy, and S. S. Kapoor, *Phys. Rev. C* **18**, 549 (1978).
 [36] D. Fabris *et al.*, *Phys. Rev. C* **50**, R1261 (1994).
 [37] W. Trautmann, O. Hansen, H. Tricoire, W. Hering, R. Ritzka, and W. Trombik, *Phys. Rev. Lett.* **53**, 1630 (1984).
 [38] H. Tricoire *et al.*, *Z. Phys. A* **306**, 127 (1982).
 [39] B. N. Kalinkin and I. Z. Petkov, *Acta Phys. Pol.* **25**, 265 (1964).
 [40] M. Blann and F. Plasil, *Phys. Rev. Lett.* **29**, 303 (1972).
 [41] K. Siwek-Wilczynska, E. H. du Marchie van Voorthuysen, J. van Popta, R. H. Siemssen, and J. Wilczynski, *Phys. Rev. Lett.* **42**, 1599 (1979).
 [42] J. Wilczynski, *Nucl. Phys. A* **216**, 386 (1973).
 [43] C. S. Palshetkar *et al.*, *Phys. Rev. C* **82**, 044608 (2010).
 [44] T. Ahmad *et al.*, *Int. J. Mod. Phys. E* **20**, 645 (2011).
 [45] S. Gupta *et al.*, *Phys. Rev. C* **61**, 064613 (2000).
 [46] K. Surendra Babu *et al.*, *J. Phys. G* **29**, 01011 (2003).
 [47] S. Mukherjee *et al.*, *Eur. Phys. J. A* **12**, 199 (2001).
 [48] U. Gupta *et al.*, *Nucl. Phys. A* **811**, 77 (2008).
 [49] P. P. Singh, B. P. Singh, M. K. Sharma, D. P. Unnati Singh, R. Prasad, R. Kumar, and K. S. Golda, *Phys. Rev. C* **77**, 014607 (2008).
 [50] D. P. Singh *et al.*, *Phys. Rev. C* **80**, 014601 (2009).
 [51] R. A. Broglia and A. Winther, *Elastic and Inelastic Reactions*, Heavy Ion Reaction Lecture Notes Vol. I (Benjamin Cummings, Redwood City, CA, 1981), p. 114.
 [52] C. Y. Wong, *Phys. Rev. Lett.* **31**, 766 (1973).
 [53] H. Morgenstern *et al.*, *Phys. Lett. B* **113**, 463 (1982).
 [54] D. J. Hinde, M. Dasgupta, B. R. Fulton, C. R. Morton, R. J. Wooliscroft, A. C. Berriman, and K. Hagino, *Phys. Rev. Lett.* **89**, 272701 (2002).
 [55] M. A. Candido Ribeiro, L. C. Chamon, D. Pereira, M. S. Hussein, and D. Galetti, *Phys. Rev. Lett.* **78**, 3270 (1997).
 [56] P. R. Christensen and A. Winther, *Phys. Lett. B* **65**, 19 (1976).
 [57] D. Singh *et al.*, *J. Phys. Soc. Jpn.* **75**, 104201 (2009).
 [58] D. P. Singh, V. R. Sharma, A. Yadav, P. P. Singh, M. K. Unnati Sharma, R. Kumar, B. P. Singh, and R. Prasad, *Phys. Rev. C* **89**, 024612 (2014).
 [59] U. Gupta *et al.*, *Phys. Rev. C* **80**, 024613 (2009).
 [60] S. Mukherjee *et al.*, *Int. J. Mod. Phys. E* **15**, 237 (2006).